Biomechanical model of batoid (skates and rays) pectoral fins predicts the influence of skeletal structure on fin kinematics: implications for bio-inspired design

2015 Bioinspir. Biomim. 10 046002

(http://iopscience.iop.org/1748-3190/10/4/046002)

Bioinspiration & Biomimetics

RECEIVED
17 September 2014

REVISED
1 May 2015

ACCEPTED FOR PUBLICATION
8 May 2015

PUBLISHED
16 June 2015

PAPER

Biomechanical model of batoid (skates and rays) pectoral fins predicts the influence of skeletal structure on fin kinematics: implications for bio-inspired design

R S Russo[1,3], S S Blemker[1,2], F E Fish[4] and H Bart-Smith[3]

[1] Multi-Scale Muscle Mechanics Lab, Department of Mechanical & Aerospace Engineering, University of Virginia, Charlottesville, VA 22904, USA
[2] Multi-Scale Muscle Mechanics Lab, Department of Biomedical Engineering, University of Virginia, Charlottesville, VA 22904, USA
[3] Bio-inspired Engineering Research Lab, Department of Mechanical & Aerospace Engineering, University of Virginia, Charlottesville, VA 22904, USA
[4] Liquid Life Lab, Department of Biology, West Chester University, West Chester, PA 19383, USA

E-mail: hb8h@virginia.edu

Keywords: batoids pectoral fin, cartilage structure, kinematics

Abstract

Growing interest in the development of bio-inspired autonomous underwater vehicles (AUVs) has motivated research in understanding the mechanisms behind the propulsion systems of marine animals. For example, the locomotive behavior of rays (Batoidea) by movement of the pectoral fins is of particular interest due to their superior performance characteristics over contemporary AUV propulsion systems. To better understand the mechanics of pectoral fin propulsion, this paper introduces a biomechanical model that simulates how batoid skeletal structures function to achieve the swimming locomotion observed in nature. Two rays were studied, *Dasyatis sabina* (Atlantic ray), and *Rhinoptera bonasus* (cownose ray). These species were selected because they exhibit very different swimming styles (undulation versus oscillation), but all use primarily their pectoral fins for propulsion (unlike electric rays or guitarfishes). Computerized tomography scans of each species were taken to image the underlying structure, which reveal a complex system of cartilaginous joints and linkages. Data collected from these images were used to quantify the complete skeletal morphometry of each batoid fin. Morphological differences were identified in the internal cartilage arrangement between each species including variations in the orientation of the skeletal elements, or radials, and the joint patterns between them, called the inter-radial joint pattern. These data were used as the primary input into the biomechanical model to couple a given ray skeletal structure with various swimming motions. A key output of the model is an estimation of the uniaxial strain that develops in the skeletal connective tissue in order for the structure to achieve motions observed during swimming. Tensile load tests of this connective tissue were conducted to further investigate the implications of the material strain predictions. The model also demonstrates that changes in the skeletal architecture (e.g., joint positioning) will effect fin deformation characteristics. Ultimately, the results of this study can be used to guide the design of optimally performing bio-inspired AUVs.

1. Introduction

Batoid rays are cartilaginous fishes with dorsaventrally flattened bodies and pectoral fins that are greatly expanded and fused to the head [1]. Rays use their pectoral fins exclusively for propulsion [2, 3], where fin motion ranges across species from oscillation to undulation [4–6]. Rosenberger [1] developed a description of ray swimming called the 'swimming mode continuum', which characterizes any ray's pectoral fin motion by the number of undulatory waves (referred to as the undulatory wave number) that travel along the chord of the fin. Based on this description, rays with a wave number below 0.5 are categorized as oscillators and rays with a wave number of 1.0 or higher are undulators [1].

Across different ray species, the swimming style continuum has been shown to correlate with planform shape. The fin planform of rays ranges from rhomboidal to circular [1, 7], which correlates with oscillatory to undulatory motion, respectively [1]. Rays with more circular planforms tend to use undulation for propulsion and generally swim slowly at about one body length per second or less. They are observed to have excellent low speed maneuverability and spend much of their time on the sea bottom [1, 8]. Those with more rhomboidal, or triangular, planforms tend to employ oscillation, swim faster (swimming up to three body lengths per second or faster in bursts), exhibit more migratory behavior, and spend much of their time swimming in the water column [1, 2]. Although variations in the swimming style in rays have been identified, as well as associated differences in their swimming performance [1, 2], the mechanisms behind such motions are not well understood.

The fins of batoids are composed of an array of approximately 100–200 cartilage segments connected in series by joints to form finger-like structures called radial elements (figure 1(b)) [9]. These radial elements originate at the root of the fin and extend outward to the edge of the fin, repeating down the ray body and serve as structural support [9]. Mechanical connections exist between the radial elements in the form of cartilaginous 'cross-bracing' connective tissue [9]. As will be shown, the connective tissue can have a significant influence on the range of motion of adjacent radial elements. All rays have these features; however, the assembly of these components was shown to vary across species [9]. For example, radial element lengths, orientations, and internal joint patterns between radial elements have been shown to vary across species [9]. Though these variations in the skeletal design were identified, it is currently unclear how these variations effect ray locomotion.

The purpose of this study is to determine the influence of the underlying skeletal arrangement, connective tissue, and planform shape on ray pectoral fin kinematics. A computational model has been developed that allows us to isolate the effects of each of these features, which can provide key insights into the kinematics of different species, a study which would be impossible to perform experimentally. The specific objectives of this paper were to develop a biomechanical model—validated through *in vivo* ray swimming comparisons and computerized tomography (CT) imaging—to simulate the ray skeletal structure kinematics to achieve specific ray locomotion and to use the model to explore the role of skeletal architecture and planform shape on fin kinematics. Specifically, the joint displacements and mechanical strain between adjacent radials within the fin are quantified when forced to perform a range of motions. Our primary hypothesis is that both the skeletal arrangement and the tensile properties of the cartilaginous cross-braces influence the desired kinematics of the pectoral fin by limiting the ability of adjacent radials to move relative to one another. Additionally, we hypothesize that differences in the tensile properties of the cross-braces occurs between the species and vary spatially within a species to accommodate these desired kinematics. Data from these tests provide insight into the limitations into the kinematic motion possible for a prescribed cartilage arrangement.

Ultimately, insights gained from this work will be used to inform the mechanical design of artificial pectoral fins for the propulsion systems of autonomous underwater vehicles (AUVs). Understanding of the constraints on movements of the propulsors for bio-inspired AUVs can shorten development time and enhance vehicle locomotor performance.

2. Experimental studies

For this study, two species of rays were selected: Atlantic stingray (*Dasyatis sabina*) and cownose ray (*Rhinoptera bonasus*). Both rays belong to the taxonomic group Batoidea [5]; however, they are at opposite ends of the swimming mode continuum [1]. The cownose ray is considered to be an oscillator and the Atlantic ray an undulator [1, 2]. By choosing species that are taxonomically related, but exhibit different swimming styles, the kinematic differences between the two species can be constrained to just those movements related to pectoral fin morphology.

A series of CT scans were taken at the Computerized Scanning and Imaging Facility of Woods Hole Oceanographic Institution to create a three-dimensional (3D) reconstruction of the underlying cartilage for the Atlantic and cownose rays (figure 1). Scans were taken with their bodies flattened against the scanning platform as in an *in vivo* rest position. The cownose ray specimen was approximately 344 mm in chord-length and 279 mm in span, and the Atlantic ray specimen was 343 mm in chord-length and 162 mm in span, where span is measured from the body midline to the fin tip. The scans were taken along the span of each ray on a Siemens volume zoom CT scanner, beginning at one fin tip and progressing over the entire body to the other fin tip. Spiral protocols for data acquisitions with 100 mAs, 120 kV, 0.5 detector collimation at 0.5 mm s^{-1} table feeds and 1 s tube rotations were used. All images were reconstructed in both soft tissue (U40u) and ultra-high resolution (U90u) kernels. 3D reconstructions of the ray skeleton were digitally rendered from the DICOM images of the CT scans using Osirix Imaging Software (Advanced Open-Source PACS Workstation DICOM Viewer, www.osirix-viewer.com). For each specimen, the 3D location of each cartilage joint was manually digitized based on the 3D reconstructions in Osirix (figure 1). Using the joint location obtained from the CT data, the connectivity of each cartilage element is the foundation of the biomechanical model (figure 2(a)).

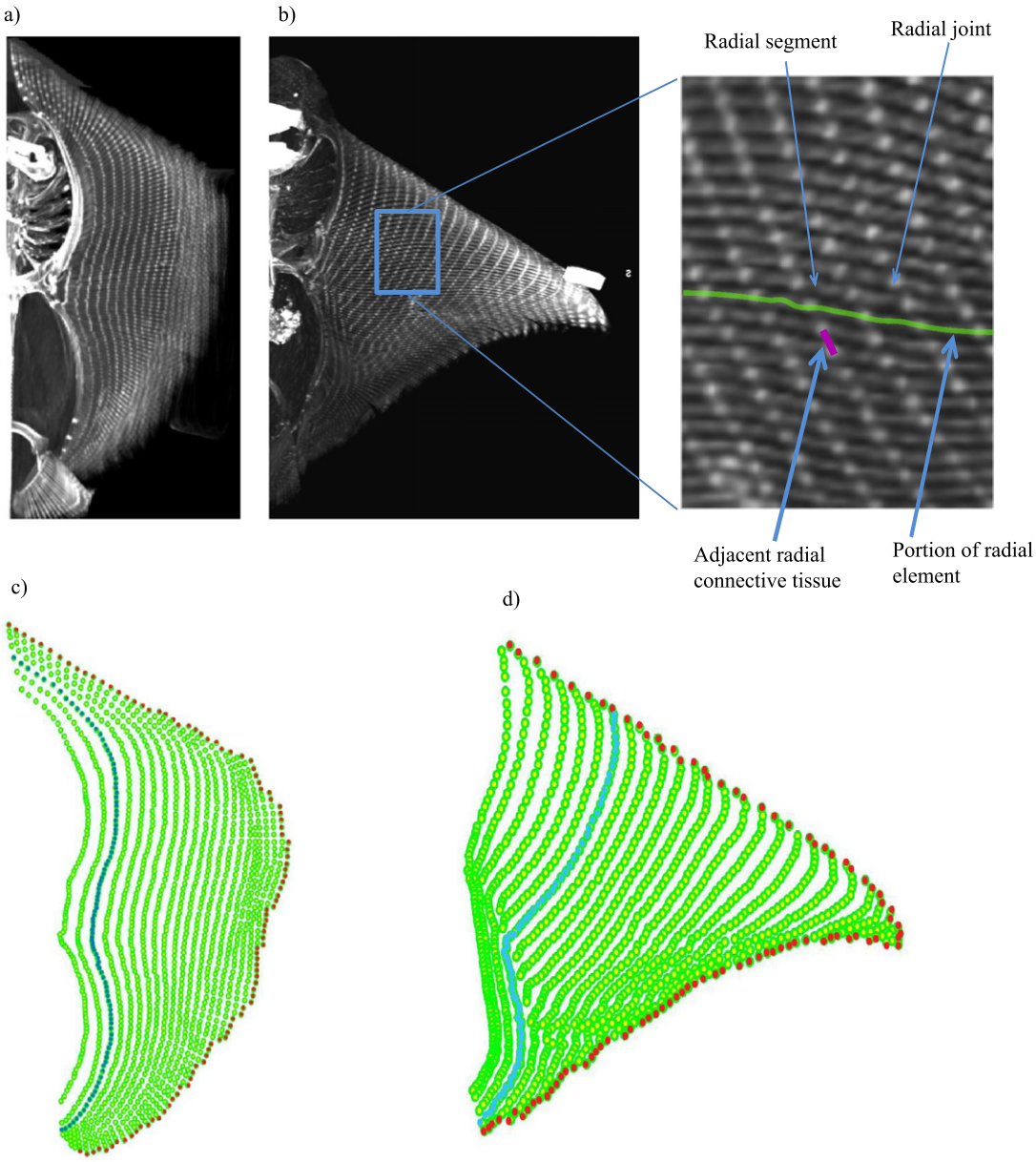

Figure 1. Reconstructed CT images of the Atlantic ray (a) and cownose ray (b) viewed from the dorsal perspective to reveal the anatomical components of the skeleton including radial segments, joints, and adjacent radial connective tissue. Skeletal morphometry was quantified by digitizing CT images and obtaining the coordinates of cartilage joint positions (c) and (d)—green. Skeletal patterns were identified from the images including planform (red), and inter-radial joint pattern (IRJP) (blue).

In addition to quantifying the spatial arrangement of the cartilage elements and joints, an experimental study was carried out to measure the tensile response of the connective tissue present between the radials. In order to determine the physiological strain limit (i.e., the amount of strain that can be accommodated as one radial moves relative to its neighbor) of cross-bracing, uniaxial tensile tests were carried out to quantify the failure strain of the adjacent radial connective tissue at various locations within the pectoral fin. Sections of the underlying cartilage were dissected from cownose ray ($n = 4$) and Atlantic ray ($n = 5$) fin specimens for mechanical load testing. These samples were dissected into dog bone samples following protocols by standard ISO 527-4. The ray skin and muscle was removed from the ray skeleton leaving behind just the radial elements with adjacent radial connective tissue still intact. The whole cartilage structure was segmented into samples for testing (figure 3(a)). The ends of the cartilage samples were inserted into clamps that were custom manufactured using a Dimension 1200es Series 3D-printer and were made compatible with an Instron microtester (figure 3(a)). Tensile loading was applied to the cartilage section perpendicular to the long axis of the cartilage segments, resulting in uniaxial straining of the adjacent radial connective tissue. Loading continued until failure of the connective tissue was reached. Load was measured via a 500 N capacity load cell and displacement measurements were recorded by tracking displacement between two

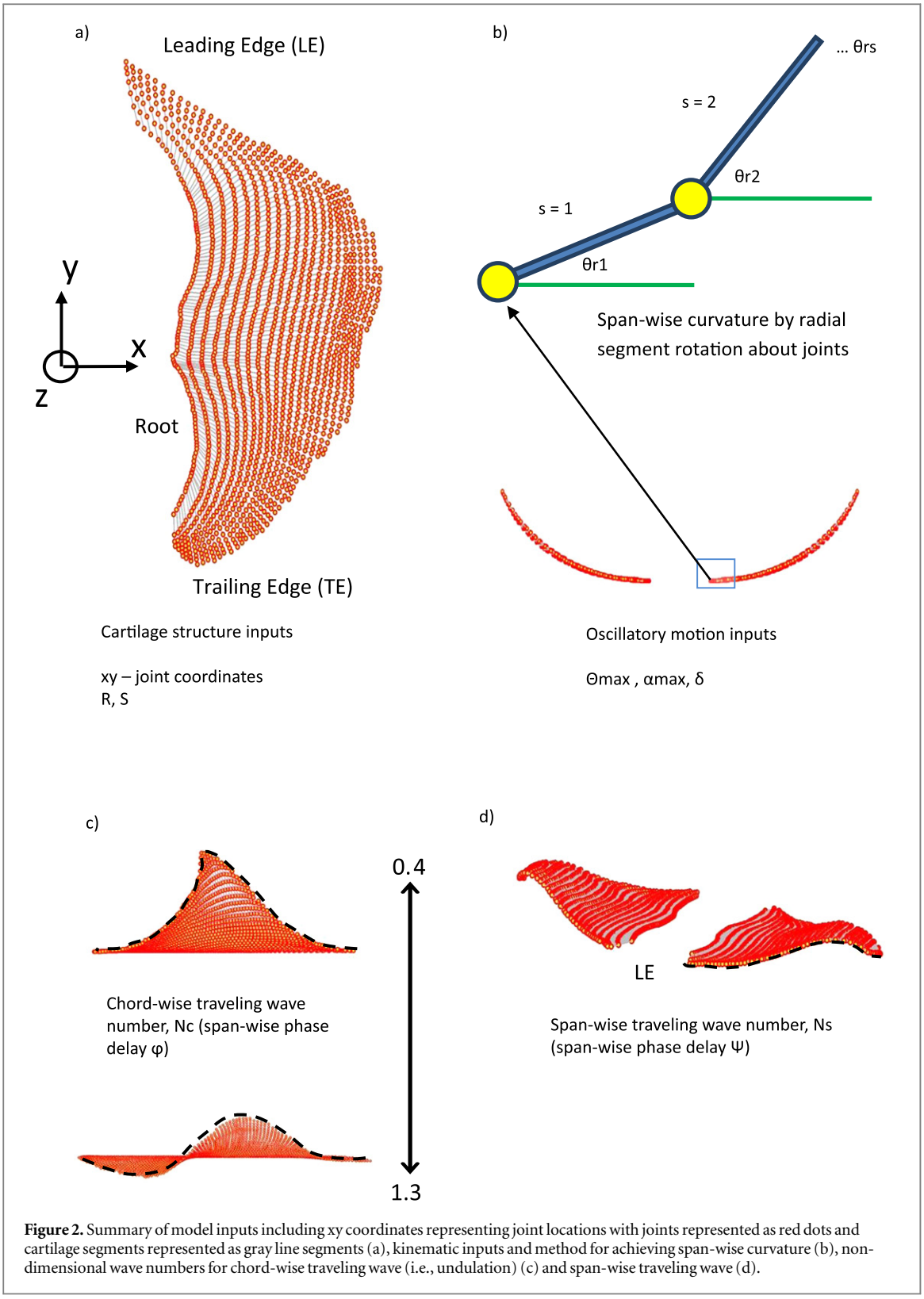

Figure 2. Summary of model inputs including xy coordinates representing joint locations with joints represented as red dots and cartilage segments represented as gray line segments (a), kinematic inputs and method for achieving span-wise curvature (b), non-dimensional wave numbers for chord-wise traveling wave (i.e., undulation) (c) and span-wise traveling wave (d).

reflective tags using a laser extensometer (figure 3(b)) calibrated for a tag displacement range of 0–5 mm. These tags were located far enough away from the clamps to avoid localized effects of the clamps and also to exclude grip slippage displacements from the measurements. Several cartilage samples were extracted from each fin at different locations so that the variation in strain thresholds in the fin could be determined. The gauge length at the fin root of the cownose ray specimens was approximately 42 ± 2 cm. Each of the Atlantic ray specimens had a gauge length of approximately 20 ± 2 cm. The samples were tested at a crosshead displacement rate of 0.001 mm s^{-1}. The cownose ray specimens, being considerably larger than the Atlantic rays, provided 10 samples per fin and the Atlantic ray provided 4 samples per fin. Failure was determined as the

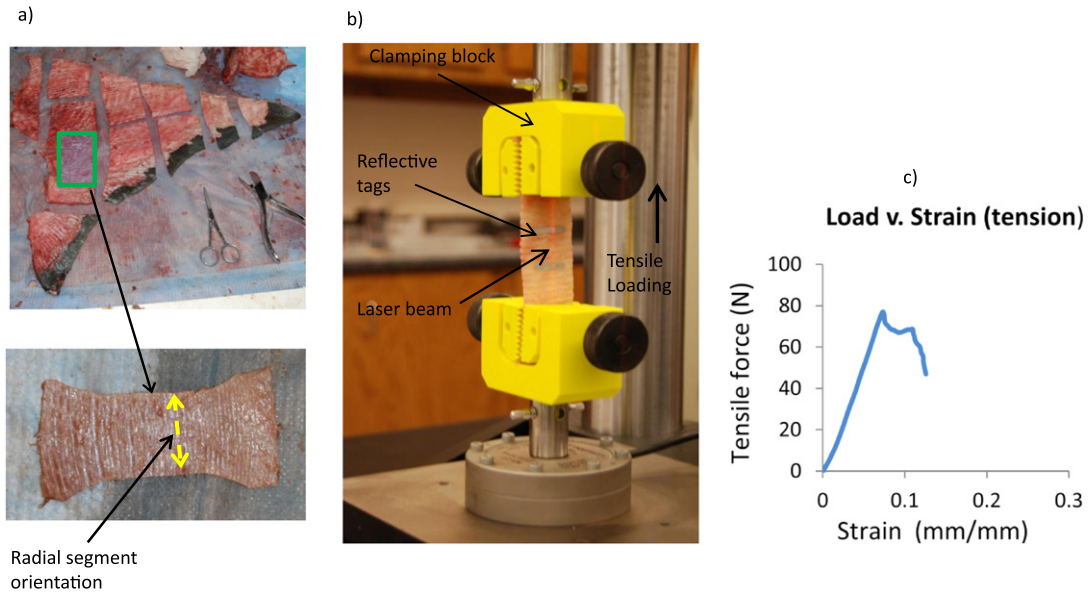

Figure 3. Samples of cartilage were dissected out of the ray (a) and inserted into a custom testing apparatus (b). Tension was applied in the direction perpendicular to the radial segments long axis ((a)-yellow). Load and displacement measurements were taken with load measured using built in load cells and displacement measured using a laser extensometer in which a laser beam is used to track distance between two reflective tags. Force and strain data were acquired for analysis (c).

point at which the load dropped to 40% of the peak load and in all samples was observed to occur within the gauge length. In order to test the hypothesis that the average strain threshold differed between species, we performed a two-sample t-test comparing in the mean strain limit values between the two species. A one-way ANOVA was performed within each species in order to test the hypothesis that the strain threshold varied across regions in each species.

3. Biomechanical model

The joint location and connectivity information obtained from the CT data was used to define the skeletal morphometry and initial joint positions in the biomechanical model (figure 2(a)). The model solves for the joint and segment trajectories based on a set of time-varying input control parameters to predict the resulting time-varying 3D changes in shape of the entire fin. Joint positions were described using a Cartesian coordinate system with coordinates (x,y,z), with the x and y axes corresponding to the span-wise and chord-wise directions of the fin, respectively (figure 2(a)). The model was validated by comparing the resultant outputs from the model to videography of rays swimming. The results from the model are then used to predict the axial strains that develop between adjacent radials, which can be compared with the connective tissue tensile test results.

3.1. Kinematic definition

The time-varying input control parameters were defined to capture the dominant characteristics of ray locomotion, which include span-wise curvature, chord-wise traveling wave [1, 10–12], and span-wise traveling wave (figures 2(b)–(d)). To generate motion, a set of deflection angles for each radial segment is calculated over time ($\theta_{rs}(t)$). Non-dimensional wave numbers—i.e. number of waves along a defined direction—are used for prescribing the chord-wise (N_c) and span-wise (N_s) undulation. These non-dimensional wave numbers are used for calculating angular phases required for simulating traveling wave motion. The oscillatory component is determined by the amplitude of oscillation, θ_{max}, and the oscillation frequency, ω

$$\theta_{rs}(t) = s\theta_{max}\sin(\Phi r + \Psi s - \omega t) + \delta s, \quad (1)$$

$$\Phi = \frac{2\pi N_c}{R}, \quad (2)$$

$$\Psi = \frac{2\pi N_s}{S}. \quad (3)$$

R and S are the total number of radial elements and segments of the longest radial element, respectively. The indices r and s denote the position of cartilage segment, s, relative to the fin root of radial element, r, relative to the leading edge. N_c refers to the number of waves traveling along the chord of the fin, while N_s is the span-wise traveling wave number. Both N_c and N_s are kinematic variables used for calculating time independent angular phases Φ and Ψ to achieve traveling wave motion. A scalar term, δ, is included for achieving asymmetric flapping where any non-zero value of δ will result in a vertical shift in the y-axis of the deflection angle control signal. The matrix of joint angles $\theta_{rs}(t)$ is then used to calculate the xyz joint displacements from the following expressions beginning with $s = 2$ and extending out along each radial element r

$$x_{rs} = L_{rs} \cos[\theta_{rs}(t)] \sin\left[\beta_{rs}\right] + x_{r,(s-1)}(t), \quad (4)$$

$$y_{rs} = L_{rs} \cos[\theta_{rs}(t)] \cos\left[\beta_{rs}\right] + y_{r,(s-1)}(t), \quad (5)$$

$$z_{rs} = L_{rs} \sin[\theta_{rs}(t)] + z_{r,(s-1)}(t). \quad (6)$$

The matrices L and β are radial segment length and transverse segment angle respectively, where the transverse angle refers to the angle of the cartilage segment rs in the xy-plane relative to the y-axis. This information is obtained directly from the CT scans. In this model, the cartilage segments are represented as rigid bodies and the nodes are represented as hinge joints constrained to a single rotational degree of freedom (figure 2(b)), and are based on the values of L and β defined when the fin is at rest. These two assumptions give rise to the system's kinematic constraints and are essential to solving the kinematics. The algorithm was input into MATLAB to solve for the time-varying positions of each joint.

The rigid body/hinge joint assumptions were validated via further CT imaging. The two species of rays were scanned both in a flat and a deformed configuration. For the deformed configuration, the fins of each ray were placed into a position with the fin flexed upward, similar to the maximum upward displacement that occurs during swimming (figure 6). This configuration was chosen to simulate the most extreme deformations that could be achieved by the fin *in vivo*. This is not an extreme bending condition but is sufficient to test the plausibility of cartilage element bending during swimming. The fully flexed state of the fin corresponded to an apparent non-injurious physiological limit of the fin. OsiriX Imaging Software was used to digitize the cartilage structure in both the flat and deformed configurations. To provide a quantitative assessment of rigid body/hinge joint assumptions, a rigid body rotation analysis was performed for one particular radial. The spatial coordinates (xyz) of each cartilage joint contained within this radial were digitized from the images of the fin when flat and in the deformed configuration. The biomechanical model was used to assess the validity of the rigid body assumption by comparing the model output (where only deflection angles were applied to each joint) with the CT images of the deformed configuration.

Video data of ray swimming was collected at West Chester University of Pennsylvania Liquid Life Laboratory and compared to the model outputs for validation. Representative examples of comparison between *in vivo* results and the model are shown in figures 4 and 5 (Atlantic ray and cownose ray, respectively). Specimens were obtained and tested in accordance with the West Chester University Institutional Animal Care and Use Committee. Measurements of vertical displacement of the fin edge for both the Atlantic and cownose rays were taken at several positions along the chord of the fin. In each case, six vertical lines spaced evenly apart along the fin chord were used to measure the edge displacement at each position. The displacement measurements were normalized by chord length to account for variations in specimen size and these results were compared with model predictions.

3.2. Strain and displacement analysis

The output from the model allows us to calculate the displacements of the joints and the resolved tensile mechanical strain generated in the connective tissue between adjacent radials. This tensile strain can be expressed as a function of the prescribed inputs for a given cartilage arrangement (figure 1(c)—magenta). Mechanical strain was calculated as:

$$\varepsilon_{rs}(t) = \frac{\left|U_{rs}(t) - U_{(r+1),s}(t) - U_{rs}(0) + U_{(r+1),s}(0)\right|}{\left|U_{rs}(0) - U_{(r+1),s}(0)\right|}, \quad (7)$$

where $U_{rs}(t)$ and $U_{rs}(0)$ are 3D vector fields that define the positions of all cartilage joints at time t and at rest respectively. The components of $U_{rs}(0)$ are obtained from the CT images and $U_{rs}(t)$ is calculated using equations (4)–(6). This is a key component of the analysis in that these predicted strains (based on the model inputs) can be compared with the measured tensile strain from the mechanical testing, described earlier. The mechanical tests results define a physiological limit to the cross bracing tissue and if the model calculates strain values close to or in excess of these limits, it can inform us about the feasibility of the design, especially as it pertains to structural perturbation studies described next.

3.3. Perturbation studies

We made use of structural perturbation studies to determine the influence of skeletal morphology on kinematics. To conduct this analysis, kinematic inputs were found for both the Atlantic and cownose rays performing their respective natural swimming gaits (figures 3 and 4). Each set of kinematics was applied to both skeletal structures, where the skeletal structure of the Atlantic ray was forced to perform motions of the cownose ray and vice versa. Perturbations to the skeletal morphology were also simulated. Here an Atlantic ray skeletal structure (figure 7(a)) was artificially altered such that the overall planform matched that of the cownose ray while preserving the Atlantic ray's internal cartilage structure (figure 7(b)). To accomplish this, radial segments and joints were added onto the edge of the naturally occurring Atlantic ray cartilage structure to alter its planform shape. Radial elements were then removed so that each structure had the same total number of radial elements. Finally, the artificial structure was scaled in both chord-wise and span-wise directions so that its span and aspect ratio matched those of the cownose ray. The displacement and strain results of this perturbation were compared to those of the original cownose ray cartilage structure (figure 7(c)).

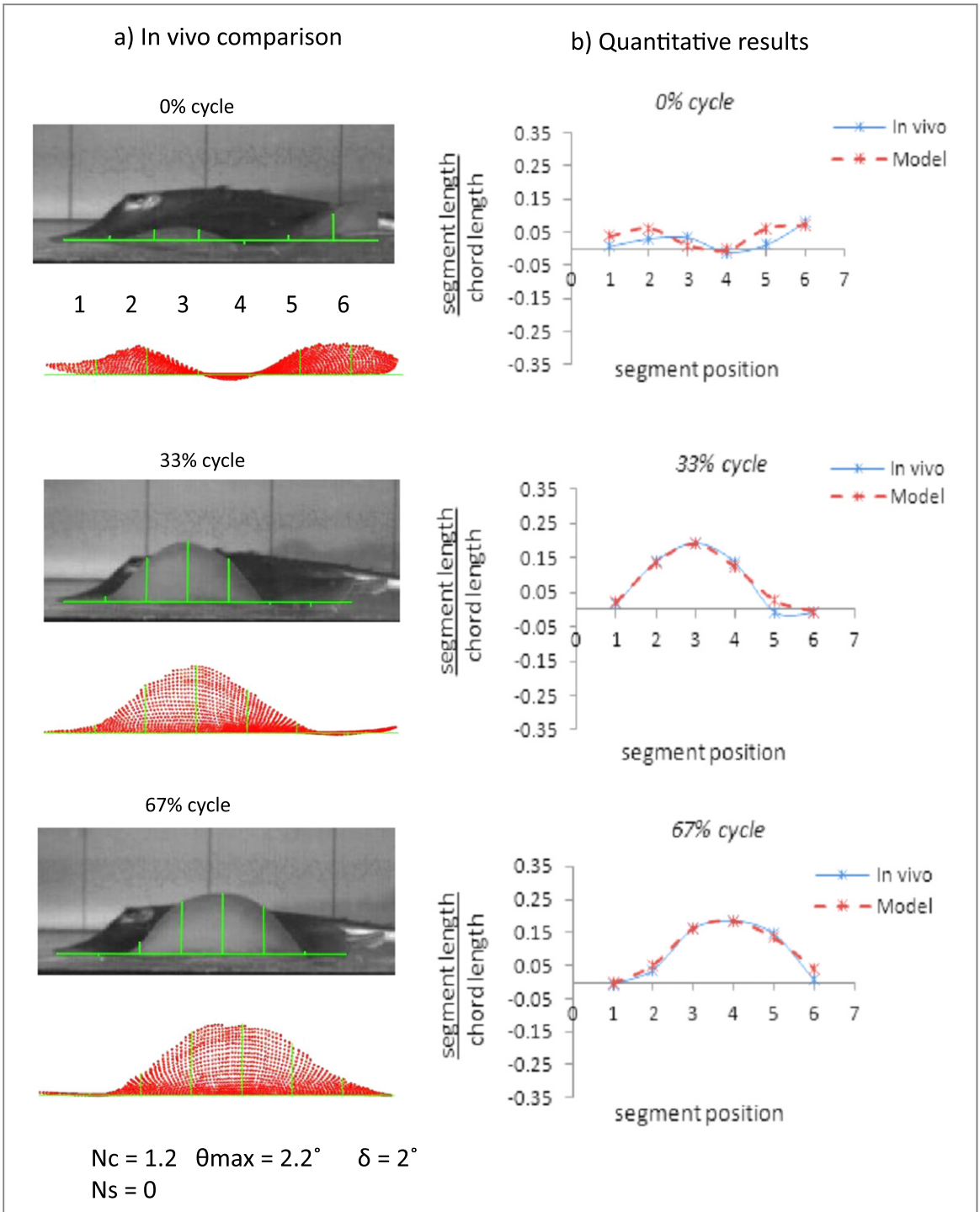

Figure 4. Comparison between the model outputs for the Atlantic ray and *in vivo* swimming data with (a) qualitative comparisons and (b) quantitative comparisons. The motion was tracked in time with three time points reported displayed as a percentage of the gait cycle.

4. Results

4.1. Validation of biomechanical model

4.1.1. Rigid body/hinge joint assumptions

The CT images taken in the flat and deformed configuration were compared with the model output, where only rotation at the joints is assumed. These results demonstrate that the cartilage segments primarily behave as rigid elements. Qualitatively, the segments were not observed to bend in order to achieve the necessary span-wise curvature (figures 8(a), (b), (e) and (f)) with deformation held to rotation at the nodes. A single radial element was sectioned out of the reconstructed CT images of the cownose ray (figures 8(a) and (b)) and Atlantic ray (figures 8(e) and (f)) in the flat and deformed configuration. Virtual representations of these two radials—flat fin in blue and in situ deformed fin in maroon—are shown in figures 8(c) and (g). Rigid body rotation was then applied to the cartilage

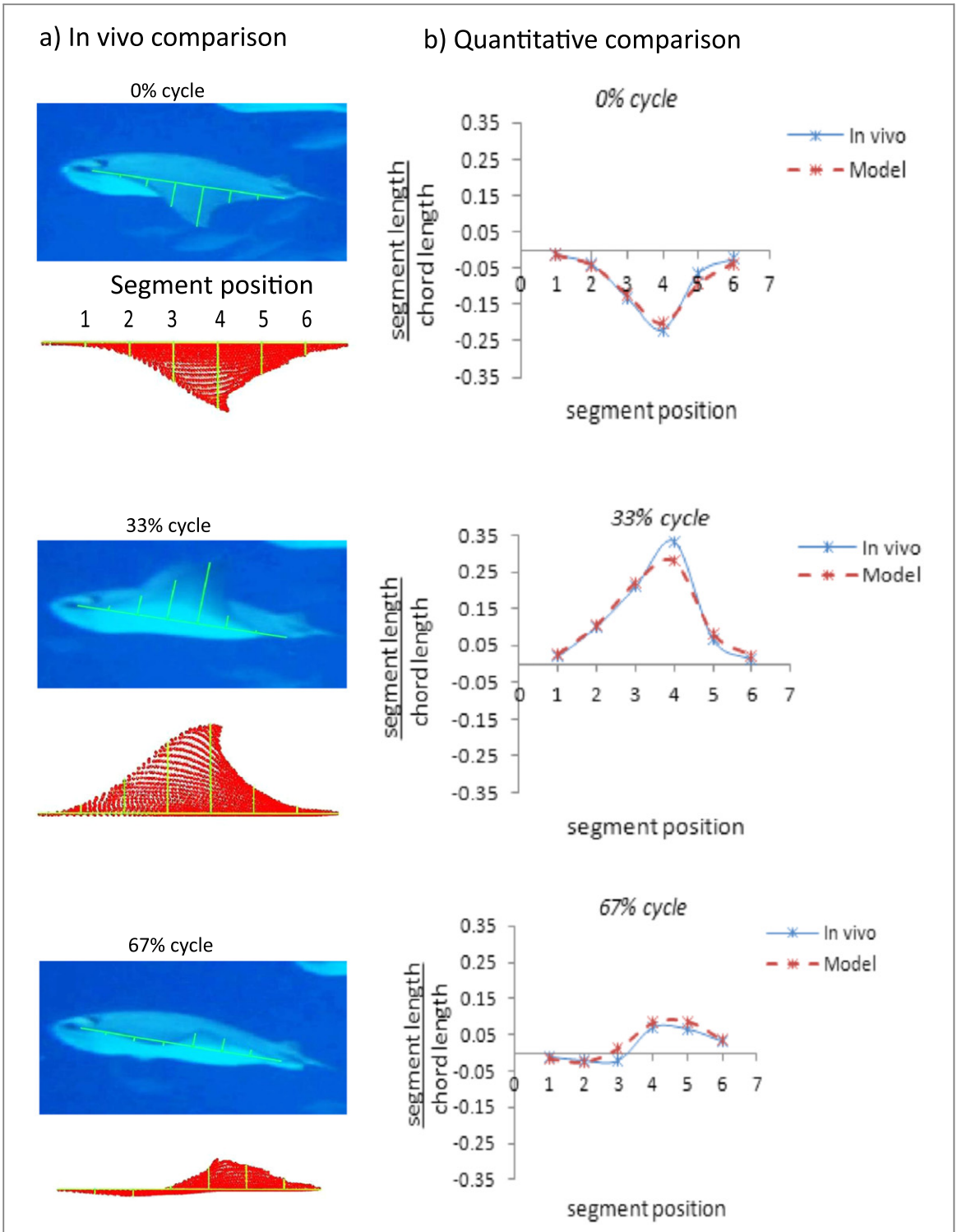

Figure 5. Comparison between the model outputs for the cownose ray and *in vivo* swimming data with (a) qualitative comparisons and (b) quantitative comparisons.

segments of the flat radial element such that the radial element from the flat case matched the curvature of the radial element of the deformed case (figures 8(d) and (h)). Critically, the difference between the rigid-body model predictions and the observed kinematics was less than 2% for both the cownose ray and the Atlantic ray. The quantitative assessment demonstrates that the model, with its rigid body assumption, provides high-level agreement with the biologically derived data. It is important to note that an implicit assumption at the onset of this part of the study was that the cartilage elements were under zero strain while in the flat position. This is proven reasonable given the validation of the rigid body assumption for these elements.

4.1.2. Kinematic comparison

Table 1 gives the model inputs that result in a close match between the kinematic outputs and the *in vivo* ray swimming measurements for both the Atlantic

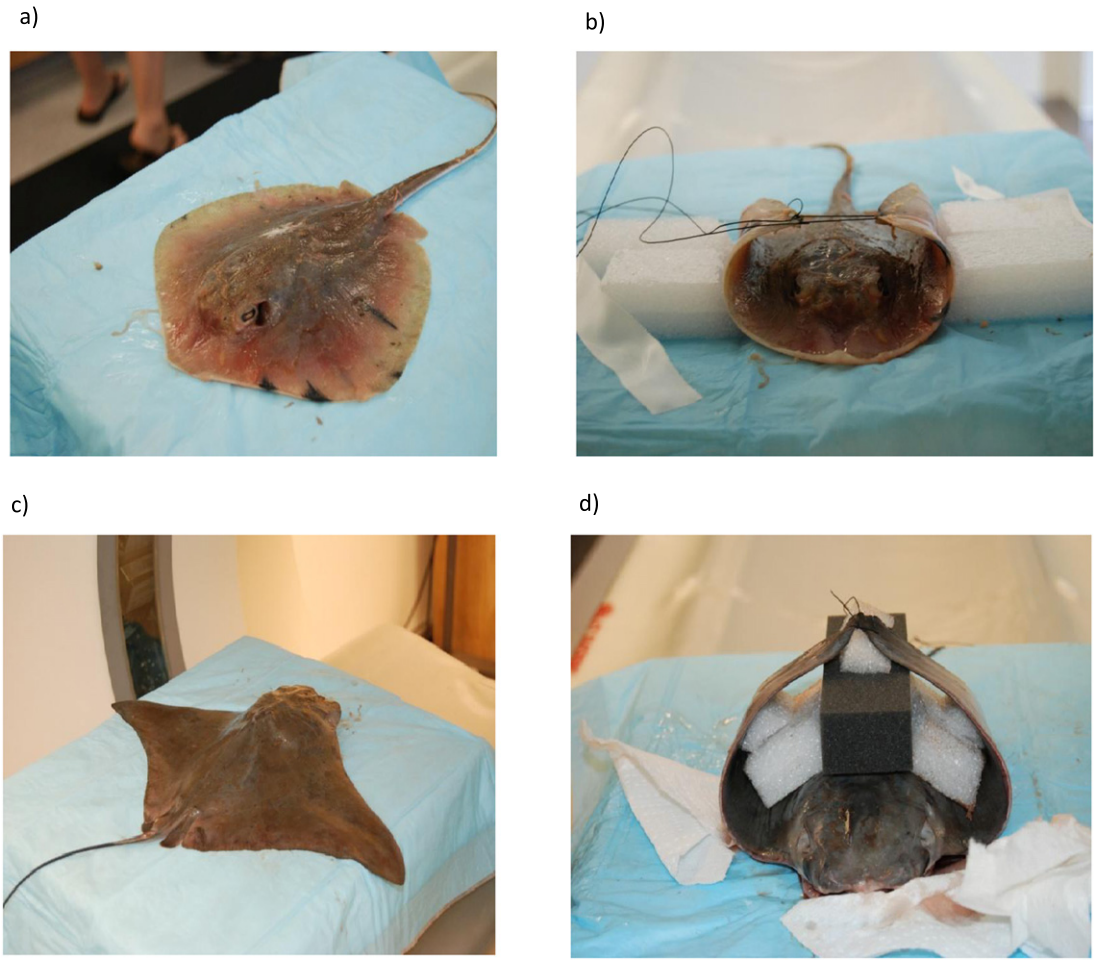

Figure 6. Model assumption validation by scanning each ray species with its fins flat against the scanning table and deformed. The Atlantic ray (a), (b) and cownose ray (c), (d) with their fins deformed (b), (d) and held together with foam blocks and surgical sutures while being passed through the CT scanner. This process was done to test the rigid body segment assumption and hinge joint assumption.

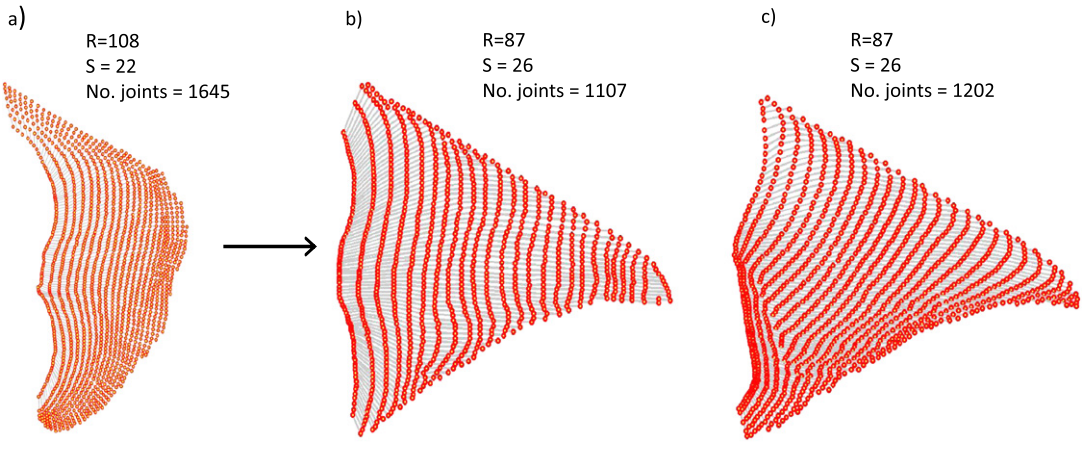

Figure 7. Morphology perturbation study process which began with the unaltered Atlantic ray structure (a), added on segments and joints to alter the planform (b), and scaled to match the fin-span and aspect ratio of the unaltered cownose ray structure (c).

and cownose rays, subject to the limitations in resolution of the videography available. These are consistent with previous descriptions of the swimming characteristics of both rays [1, 9]. The cownose ray required equal parts span- and chord-wise traveling wave numbers while no span-wise traveling wave was required for the Atlantic ray to match the *in vivo* data. Asymmetric flapping was observed for both species

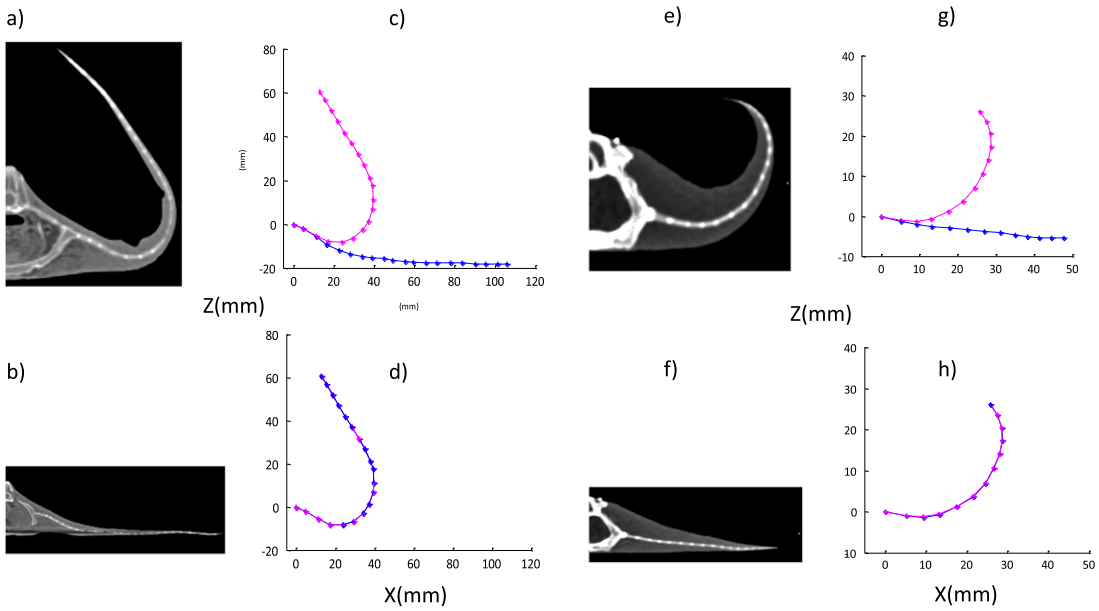

Figure 8. Single radial elements sectioned out of the reconstructed CT images of the Cownose ray (a), (b) and Atlantic ray (e), (f) with virtual representations of the radial element from the flat fin (blue) and the *in situ* deformed fin (maroon). Both cases for each species were plotted against one another (c), (g). Rigid body rotation was then applied to the radial segments of the flat radial element such that the radial element from the flat case matched the curvature of the radial element of the deformed case (d), (h).

Table 1. Biomechanical model input parameters.

Kinematic parameter	Cownose ray	Atlantic ray
Amplitude of oscillation (θ_{max})	1.45°	2.20°
Chord-wise traveling wave number (N_c)	0.2	1.2
Span-wise traveling wave number (N_s)	0.2	0.0
Asymmetric shift (δ)	0.5°	2.0°

with approximately a 2:1 ratio of upward flap to downward flap for the cownose ray and nearly upward flap only for the Atlantic ray. The error between the measured displacements and the model predictions were 4.3% for the cownose ray and 8.4% for the Atlantic ray, where percent values are obtained by calculating displacement error and normalizing by flapping amplitude (figures 4 and 5). The validation of the kinematic model and the underlying assumptions give confidence in its utility in studying the form-function relationship of the skeletal structure.

4.2. Biomaterial testing

The results from material testing reveal differences in stiffness of the connective tissue present between adjacent radial elements *within* a pectoral fin and *between* species (figure 9). The average strain threshold for the cownose ray (9.89%; *standard deviation*: 2.64%) was statistically significantly lower than that of the Atlantic stingray (16.52%; *standard deviation*: 5.01%). The 'threshold' refers to the strain level where failure occurs. Compliance of the connective tissue of the cownose ray increased from leading to trailing edges for more proximal regions of the fin. Slight increases in strain threshold were seen also toward the most distal regions of the fin (figure 9(a)). For both the cownose ray and the Atlantic stingray, the region near the tip of the fin (region 4) exhibited a statistically significantly higher strain threshold as compare to the other regions (figure 9(b)). These physiological strain limits are used to determine the kinematic limits of a given skeletal structure, and, when coupled with the strain analysis described in section 3.2, provides biological grounding when interpreting results from the biomechanical model.

4.3. Displacement, strain, and perturbation analyses

Both the nodal displacements and strain profiles were calculated for both skeletal structures using the associated kinematic inputs given in table 1. The results demonstrate different displacement and strain profiles between the two species. For the cownose ray, the adjacent radial strains were relatively uniform, where the majority of peak adjacent radial strain levels were less than 5% (figure 10(d)), which was well under the measured maximum strain threshold of ~10% (figure 9(a)). Upon closer inspection, the induced strain between adjacent radial elements in the vicinity of the fin tip reaches the threshold value but does not exceed this value. With respect to the Atlantic ray, the calculated strain generated between the radials is relatively non-uniform (figure 10(b)). The maximum value of induced strain between adjacent radials—located near the fin tip toward the trailing edge—is below the experimentally measured threshold. It also must be noted that this region coincides with the region of highest measured connective tissue compliance (figure 9(b)).

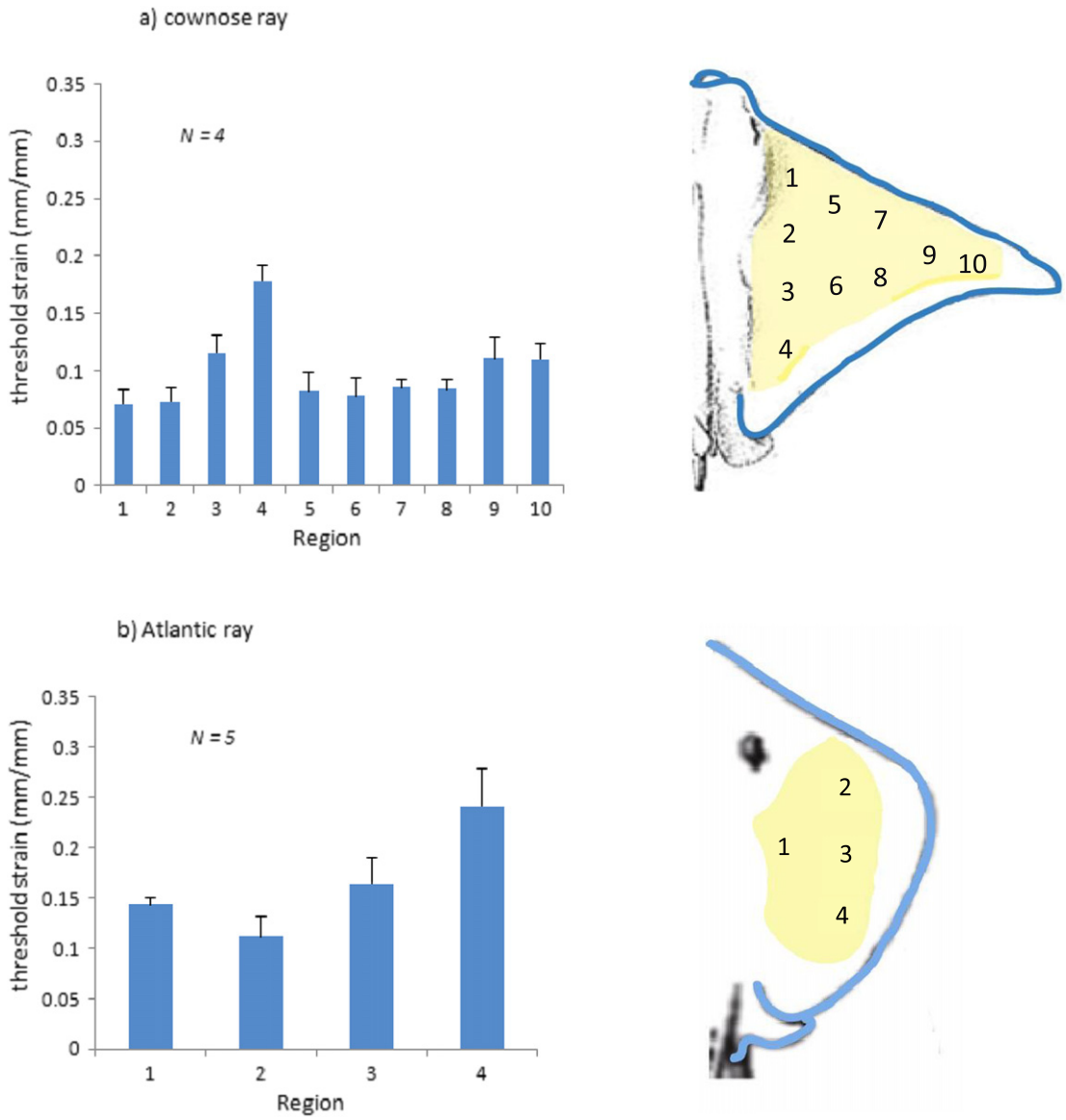

Figure 9. Results of material tests of the adjacent radial connective tissue with strain thresholds reported in accordance with position throughout the fin. Tests were performed on four cownose ray fins at ten locations (a) and on five Atlantic ray fins at four locations (b). Samples were taken from the shaded yellow regions, with specific areas label by numbers that correspond to bar graphs.

For the first perturbation analysis, the kinematic inputs for both batoid rays were switched with one another (table 1). Visually, the nodal displacements observed for the cownose ray structure, while being controlled with the inputs for the Atlantic ray, are very different to those produced when the cownose ray inputs are used (figures 10(a) and (c)). An interesting result from this analysis is when one calculates the induced strain that develops between adjacent radials. In this example, the calculated adjacent radial strain was well in excess of the measured threshold strain for approximately 34% of the cownose ray fin area (circled in red in figure 10(b)). By contrast, when the kinematic inputs of the cownose ray were prescribed to the Atlantic ray structure, the calculated strains between adjacent radials did not reach the maximum threshold strain measured experimentally (figure 10(d)).

The second perturbation analysis considers the effect of coupling the skeletal arrangement and planform shape. In this case, the structure of the cownose ray was perturbed such that it retains the cownose planform shape, yet incorporates the Atlantic ray internal joint arrangement. The displacement and strain results are greatly influenced when a particular underlying structure is *forced* into a planform shape. In the examples presented it was found that the vertical displacement for the cownose ray is directed more toward the trailing edge, with approximately 30 mm of vertical joint displacement at the mid-span trailing edge (figure 11(a)) as compared to approximately 15 mm for the perturbed Atlantic ray (figure 11(b)). One can manipulate the magnitudes of the joint displacements for the perturbed Atlantic ray at the mid-span trailing edge to better match that of the cownose ray by changing kinematic input control signals to the

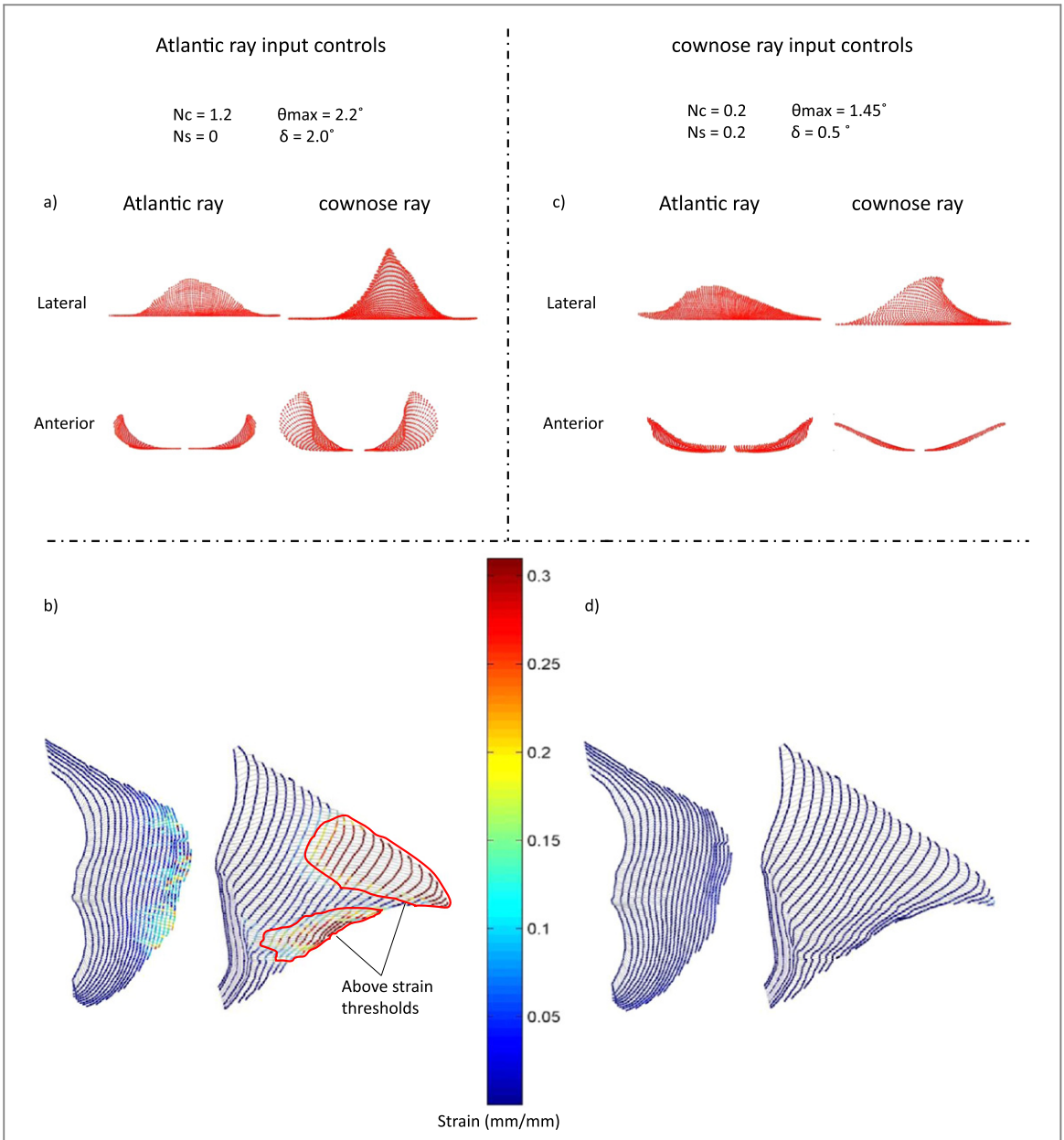

Figure 10. Motion simulations for each structure performing the motions of one another. Kinematic inputs for the Atlantic ray were applied to both structures with qualitative outputs from the model (a), and associate adjacent radial strain distribution (b). The same was repeated for the kinematic inputs for the cownose ray with qualitative outputs (c), and strain distributions (d).

biomechanical model. This was achieved by increasing the chord-wise traveling wave number from 0.2 to 0.7, and decreasing the span-wise traveling wave number to 0.0 (figure 11(c)). Critically, this cannot be done without inducing higher levels of adjacent radial strain. As can be seen, this causes the strain between adjacent radials to be far greater than the experimentally determined threshold limits found in the tension experiments.

5. Discussion

Prior studies have shown that undulation and oscillation are correlated with very different swimming performance characteristics [2, 3, 14] and body shapes [7, 9, 14], which can be incorporated into the design of an artificial fin. Techniques for simulating the motion of a fin, from both internal and external perspectives [10, 15] have been explored, but none have shown how the internal biological structure functions mechanically to create this motion. To address the mechanics of the fin motion, a biomechanical model has been developed to reproduce the swimming motions of a given batoid cartilage structure and to elucidate the role of structure on the kinematics. This computational tool can provide key insights into the link between a given structure and the resulting kinematic motions and can be used to explore this relationship to help understand the mechanisms and limitations of a particular biological foundation. It also opens up the possibility of studying skeletal configurations and kinematics not observed in nature. Critical to this endeavor was to ensure that the kinematic

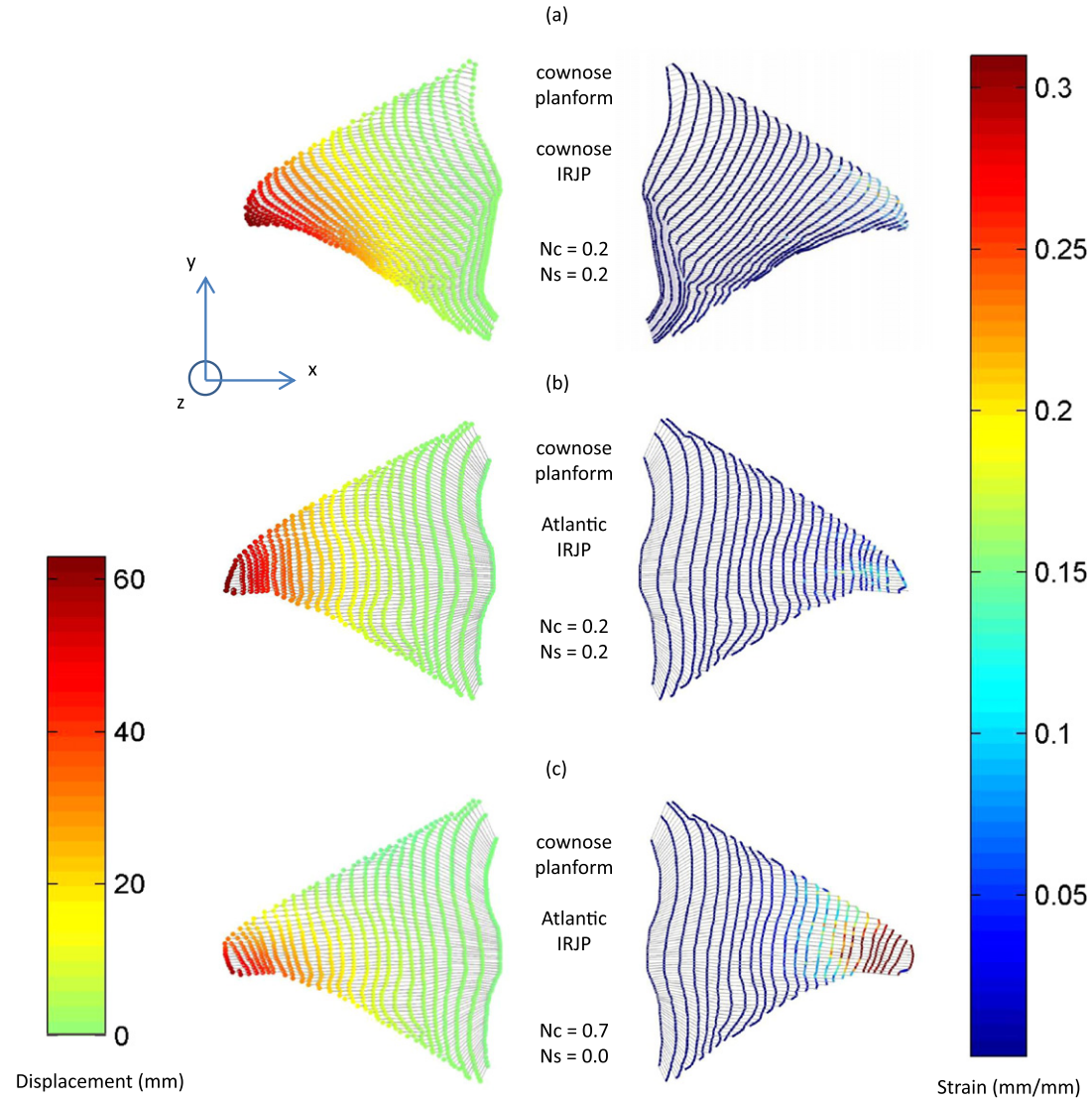

Figure 11. Perturbation study displacement plots (left) and strain plots (right) illustrating how the IRJP impacts wing deformation characteristics. The naturally occurring cownose structure (a) compared to Atlantic ray structure with the cownose planform (b) with the same kinematic inputs. Modifying the input controls to force the altered Atlantic ray structure with the cownose planform to achieve a displacement pattern closer to that of the unaltered cownose ray structure can be done, but comes at the cost of higher strain levels (c).

outputs of the model match those observed in nature. Using videography of both cownose ray and Atlantic ray, this model has been shown to accurately reproduce the natural motions of both species. Additional insight was gained by carrying out mechanical tests on biological samples from both candidate rays to test the physiological strain limits of the cross bracing between radial elements. By quantifying the threshold strain of the connective tissue, coupled with the model results, this modeling framework makes it possible to predict whether or not a prescribed motion is a feasible gait option for a given structure.

Our modeling analyses demonstrate that the interradial joint pattern (IRJP) impacts the kinematic characteristics of a fin. This is most clearly demonstrated in the perturbation study (figures 10 and 11). Coupling this information with the threshold strain data, it is now possible to predict how a particular skeletal arrangement influences the displacement–strain outputs and enables exploration of feasible configurations for biology and in the design of artificial systems. Consider for example the displacement and strain outputs for the cownose ray being controlled using either the cownose ray input parameters or the Atlantic ray input parameters. The anterior images in figures 10(a) and (c) of the cownose ray structure highlights key differences in the nodal displacements. The induced strain that develops under these conditions greatly increases when using the Atlantic ray input parameters—to values notably higher than the measured physiological limits and over a large area of the fin. These results suggest that the cownose ray would not be able to mimic the kinematic motions of the Atlantic ray. The displacement results for the Atlantic ray being controlled using cownose ray inputs show some changes but not to the extreme of the previous example. The results

highlight that the Atlantic ray structure can accommodate the input parameters to produce the kinematics of that of the cownose ray, as indicated by the fact the calculated induced strain between radials does not reach the threshold strain. Also note that strain distribution plots of the Atlantic ray performing its intended natural motion (figure 10(b)—left), when compared to the tested strain thresholds (figure 9(b)), shows that the highest strain levels correspond to the area of greatest compliance in the Atlantic ray fin (figure 9(b)). These results suggest that Atlantic ray may have evolved to accommodate this strain requirement by increasing the compliance and failure strain limits of the connective tissue in select regions.

In the second perturbation study, the IRJP was used to alter the fin flexion characteristics without requiring changes in planform or higher levels of adjacent radial strain (figure 11). For a cownose structure controlled by cownose ray inputs, the more angled IRJP, where the pattern converges toward the tail (figure 11(a)), directs the fin flexion towards the trailing edge. However, when the Atlantic ray structure is coupled with the cownose planform, the fin curls up about an axis parallel to the direction of the IRJP (figure 11(b)). Prior research on the effects of this pattern [13] agrees with this concept; however analyses involving *in situ* skeletal morphometry were not conducted, nor were adjacent radial strain levels considered. It is possible to achieve displacement profiles of the perturbed structure similar to those of the cownose ray by manipulating the input parameters (figure 11(c)—left) but this comes at the expense of higher induced strains in adjacent radials (figure 11(c)—right). This aligns with our hypothesis that the skeletal structure is influential is defining the kinematic profile potential of a given species. Also the properties of the cross bracing connective tissue does vary from the cownose ray to the Atlantic ray, which can provide kinematic displacement advantages if needed. The kinematic effects of variations in the internal cartilage arrangement will most likely have an impact on the hydrodynamic performance. However to explore this hypothesis, it will be necessary to incorporate a fluid mechanics model into the study. Future work will be done in this area to establish a link between skeletal design and swimming performance.

Prior studies have shown that undulation and oscillation are correlated with very different swimming performance characteristics [2, 3, 14] and body shapes [7, 9, 14], which can be incorporated into the design of an artificial fin. Techniques for simulating the motion of a fin, from both internal and external perspectives [10, 15] have been explored, but none have shown how the internal biological structure functions mechanically to create this motion. Through the approach presented in this study, the skeletal designs observed in nature can be explained and, where appropriate, applied to the mechanical design of artificial systems. The results of the skeletal perturbation study (figure 11) show that the input kinematics (e.g., N_c, N_s, θ_{max}) and the internal cartilage arrangement are both mechanisms for manipulating kinematic motion and so ray locomotion.

The results regarding the strain–displacement relationship, as it relates to internal cartilage arrangement, can be used to inform design of artificial structures—such as those proposed by other researchers [16–19]—to assist in achieving desired fin kinematics while keeping strain levels to a minimum. In such applications, the biomechanical model can be used to determine where high levels of compliance may be needed in an artificial fin or how rearrangement of the structure nodes can induce kinematic change without leading to an increase in fin strain. The modeling results also show that an increase in flapping amplitude of the fin tip can be achieved by either increasing the amplitude of oscillation of each segment (θ_{max}), or by holding the amplitude of oscillation constant and adding segments onto the radial elements. This approach can also be applied in cases where an increase in fin tip amplitude is desired, but the actuators at the fin root are constrained to maximum amplitude of oscillation. The CT images (figure 1) suggest that radial elements are made longer through segment addition as opposed to segment lengthening. From a kinematics perspective, this allows larger amplitude flapping without requiring higher levels of angular deflection (i.e., θ_{max}) between connecting segments of a single radial element. It is possible that the number of segments within each radial element can be set to allow for optimal muscle shortening velocity, as the muscle must shorten and lengthen as rotation about the joints occurs. This would also have an impact on the required muscle strain to accommodate the ray's swimming gaits and could be set to keep the muscle strain levels to an acceptable level.

Though many insights can be gained from modeling the kinematics of the underlying skeletal structure, there are many other factors at play with regard to the whole pectoral fin system in rays that cannot be explained using this model alone. The model demonstrates that skeletal morphology impacts kinematics of a fin, but the effect of those kinematic differences on overall system performance cannot be fully understood without considering the hydrodynamics. To understand how kinematic variations—as a result of skeletal variations—effect swimming performance, it is necessary to incorporate a computational fluid dynamics (CFD) component. The incorporation of CFD modeling will allow for the motion and morphology perturbation studies to be revisited from a hydrodynamics perspective where metrics such as thrust production, propulsive efficiency, swimming speed, and cruising economy can be used to quantify the effect of skeletal design on the whole system. Furthermore, the present model only characterizes the kinematics of the skeletal system without considering the overlaying muscle and associated force generation.

As a result, the forces required to actuate the skeletal structure when under load from fluid forces cannot be addressed. It is possible that the cartilage structure of rays is tuned to allow for efficient muscle function in addition to helping enable desirable kinematics. Investigating the muscle mechanics in addition to the skeletal kinematics is another area for exploration, which can serve to further explain biology, as well as inform the actuation systems of bioinspired AUVs.

Successfully engineering highly functioning AUVs utilizing pectoral-fin-based propulsion will require contributions from experts in both the physical and life sciences. Studying the skeletal structure of rays can be an effective route to designing underwater vehicles [20], however the level of complexity associated with biological systems is often overwhelming making it difficult or impossible to fully replicate synthetically. Despite this, principles of the biological system can still be integrated into the design of an artificial pectoral fin. The objective is to determine which features of the skeletal structure are most essential to ray swimming performance and for what reason. Once this foundation has been established, engineers can be selective in choosing which features of the biological system to leverage in the design of artificial systems. Through biomechanics, an interface is established between biology and engineering where computational modeling techniques are used to bridge the gap between biology and engineering.

Acknowledgments

The authors would like to acknowledge funding from the Office of Naval Research through the MURI program on Biologically-Inspired Autonomous Sea Vehicles (Contract No. N00014-08-1-0642; Program Office: Dr Robert Brizzolara) and the David and Lucille Packard Foundation. The authors also wish to thank the cooperation of the Computerized Scanning and Imaging Facility of Woods Hole Oceanographic Institution.

References

[1] Rosenberger L J 2001 Pectoral fin locomotion in batoid fishes: undulation versus oscillation *J. Exp. Biol.* **204** 379–94 (PMID: 11136623)

[2] Heine C 1992 Mechanics of flapping fin locomotion in the cownose ray, rhinoptera bonasus (elasmobranchii: Myliobatidae) *PhD Dissertation* Duke University, NC

[3] Klausewitz W 1963 Der lokomotionsmodus der flugelrochen (myliobatoidei) *Zool. Anz.* **173** 110–20

[4] Breder C M 1926 The locomotion of fishes *Zoologica* **50** 159–297

[5] Compagno L J V 1977 Phyletic relationships of living sharks and rays *Am. Zoologist* **17** 303–22

[6] Lindsey C C 1978 Form, function, and locomotory habits in fish *Fish Physiology* vol 7 ed W S Hoar and D J Randall (New York: Academic) pp 1–100

[7] Compagno L J V 1999 Systematics and body form *Sharks, Skates, and Rays: The Biology Of Elasmobranch Fishes* ed W C Hamlett (Baltimore, MD: Johns Hopkins University Press) pp 1–42

[8] Webb P W 1994 The biology of fish swimming *Mechanics and Physiology of Animal Swimming* ed L Maddock, Q Bone and J M V Rayner (Cambridge: Cambridge University Press) pp 45–62

[9] Schaefer J T and Summers A J 2005 Batoid wing skeletal structure: novel morphologies, mechanical implications, and phylogenetic patterns *J. Morphology* **264** 298–313

[10] Moored K W, Fish F E and Bart-Smith H Analytical model to describe pectoral fin kinematics of the manta birostris: implications for bio-inspired design in preparation

[11] Drucker G D, Walker J A and Westneat M W 2005 Mechanics of pectoral fin swimming in fishes *Fish Physiology* **23** 369–423

[12] Clark R P and Smits A J 2006 Thrust production and wake structure of batoid-inspired oscillating fin *J. Fluid Mech.* **562** 415–29

[13] Ramos E M C 2009 Mechanical investigation of a novel biomimetic morphing structure *Master's Thesis* University of California

[14] Rosenberger L J and Westneat M W 1999 Functional morphology of undulatory pectoral fin locomotion in the stingray *Taeniura lymma* (chondrichthyes: Dasyatidae) *J. Exp. Biol.* **202** 3523–39 (PMID: 10574730)

[15] Han X, Yang S and Qiu J 2009 Kinematics modeling and experiments of pectoral oscillation propulsion robotic fish *J. Bionic Eng.* **6** 174–9

[16] Moored K W and Bart-Smith H 2007 The analysis of tensegrity structures for the design of a morphing wing *J. Appl. Mech.* **74** 668

[17] Moored K W M, Smith W, Hester J M, Chang W and Bart-Smith H 2008 Investigating the thrust production of myliobatoid-inspired oscillating wing *Advances in Science and Technology Adv. Sci. Technol.* **58** 25–08

[18] Moored K W, Kemp T H, Houle N E and Bart-Smith H 2011 Analytical predictions, optimization, and design of a tensegrity-based artificial pectoral fin *Int. J. Solids Struct.* **48** 3142–59

[19] Fish F E, Haj-Hariri H, Smits A J, Bart-Smith H and Iwasaki T 2012 Biomimetic swimmer inspired by the manta ray *Biomimetics: Nature-Based Innovation* ed Y Bar-Cohen (Boca Rotan, FL: CRC Press) ch 17 pp 495–523

[20] Lynch K M and Colgate J E 2004 Mechanics and control of swimming *J. Ocean. Eng.* **29** 660–73